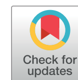

Inherent stochasticity during insulator–metal transition in VO_2

Shaobo Cheng[a,1], Min-Han Lee[b,c,1], Richard Tran[d], Yin Shi[e], Xing Li[f], Henry Navarro[c], Coline Adda[c], Qingping Meng[a], Long-Qing Chen[e], R. C. Dynes[c,2], Shyue Ping Ong[d], Ivan K. Schuller[b,c], and Yimei Zhu[a,2]

[a]Department of Condensed Matter Physics and Materials Science, Brookhaven National Laboratory, Upton, NY 11973; [b]Materials Science and Engineering Program, University of California San Diego, La Jolla, CA 92093; [c]Department of Physics, Center for Advanced Nanoscience, University of California San Diego, La Jolla, CA 92093; [d]Department of NanoEngineering, University of California San Diego, La Jolla, CA 92093; [e]Department of Materials Science and Engineering, Pennsylvania State University, University Park, PA 16802; and [f]Key Laboratory of Material Physics, Ministry of Education, School of Physics and Microelectronics, Zhengzhou University, Zhengzhou 450052, People's Republic of China

Edited by Ramamoorthy Ramesh, University of California, Berkeley, CA, and accepted by Editorial Board Member Zachery Fisk August 4, 2021 (received for review March 29, 2021)

Vanadium dioxide (VO_2), which exhibits a near-room-temperature insulator–metal transition, has great potential in applications of neuromorphic computing devices. Although its volatile switching property, which could emulate neuron spiking, has been studied widely, nanoscale studies of the structural stochasticity across the phase transition are still lacking. In this study, using in situ transmission electron microscopy and ex situ resistive switching measurement, we successfully characterized the structural phase transition between monoclinic and rutile VO_2 at local areas in planar VO_2/TiO_2 device configuration under external biasing. After each resistive switching, different VO_2 monoclinic crystal orientations are observed, forming different equilibrium states. We have evaluated a statistical cycle-to-cycle variation, demonstrated a stochastic nature of the volatile resistive switching, and presented an approach to study in-plane structural anisotropy. Our microscopic studies move a big step forward toward understanding the volatile switching mechanisms and the related applications of VO_2 as the key material of neuromorphic computing.

operando transmission electron microscopy | resistive switching | insulator–metal transition

Resistive switching in vanadium oxides has attracted much attention because of the potential applications in bioinspired neuromorphic computing and nonvolatile memories (1–4). In a basic neural network, neurons can generate nonlinear electric spikes under external excitations, while the synapses allow for the modulation of interconnected weights between neurons. In most hardware-based neuromorphic approaches, volatile switching devices (threshold switching) were used to emulate the artificial spiking neuronal behaviors, while nonvolatile switching memories were often used to mimic the synaptic functionalities (1). VO_2, whose insulator–metal transition (IMT) is above room temperature (T_{IMT} ~340 K) (5), has been widely studied as a neuristor (6). It is considered a promising candidate for energy-efficient neurons due to its threshold spiking phenomenon. In pristine VO_2 it is believed that the resistive switching can be triggered by local Joule heating across the IMT, while nonthermal switching can be induced using defect engineering (7). Recently, both volatile and nonvolatile functionalities have been achieved in VO_2 based on different switching mechanisms (8). In previous work, in situ X-ray nanomapping was used to track the out-of-plane monoclinic and rutile Bragg peaks during resistive switching (9). However, up to now the nanoscale in-plane structural anisotropy and its intrinsic stochasticity have been rarely explored (10, 11): How the system returns from metallic state to insulating state and how the structural transition influences the switching. In addition, the control of the switching usually appears to be imprecise, i.e., the voltage necessary to initiate the phase transition is not a constant (even within a single grain) (12). Therefore, it is of critical importance to understand the stochastic behavior within the neuron device and the phase transition mechanism at nanoscale under external stimuli, since the switching has to be done a large number of times during the neuron firing process. In addition, the IMT of VO_2 nanodevices can show multiple jumps, which implies that the domain structures in VO_2 may influence the transition behavior (13). Also, many physical properties, such as electrical, magnetic, and optical properties, show significant changes during the IMT process (14–16).

Here, we use in situ biasing transmission electron microscopy (TEM) with ex situ electrical transport measurement to characterize the structural phase transition across the volatile switching in VO_2. In-plane resistive switching was studied in epitaxial VO_2/TiO_2 (001) nanodevices. The original in-plane structural isotropy in the VO_2 rutile structure (R phase) will lead to anisotropy in the monoclinic phase (M1 phase) after resistive switching. Multiple monoclinic domains will form when the system returns to the insulating state. The IMT phase transition and the simultaneous electrical properties change have been systematically studied. Our results demonstrate that the structural anisotropy between different M1 VO_2 domains plays an important role in the insulating state. In addition, this study provides a thorough understanding of the volatile resistive switching process and shows that the intrinsic

APPLIED PHYSICAL SCIENCES

Significance

Emerging neuromorphic computing with resistive switching devices is one of the promising technologies toward hardware-based artificial intelligence. VO_2 has been demonstrated as a great candidate to emulate the spiking neurons because of the nature of its room-temperature metal–insulator transition and resistive switching. However, the fundamental understanding of the switching stochasticity in this strongly correlated material remains unaddressed. In this work, the inherent electrical and structural stochasticity in a VO_2/TiO_2 device has been unambiguously revealed by combining in situ transmission electron microscopy experiments and ex situ resistive switching measurement on the same device. We conclude that the randomly oriented monoclinic domains in insulating VO_2 between each resistive switching is the key factor governing the stochasticity behavior.

Author contributions: S.C., M.-H.L., X.L., R.C.D., I.K.S., and Y.Z. designed research; S.C., M.-H.L., X.L., H.N., C.A., and Q.M. performed research; R.T. and S.P.O. conducted the DFT calculations; Y.S. and L.-Q.C. carried out the phase field calculations; S.C., M.-H.L., R.C.D., I.K.S., and Y.Z analyzed data; and S.C. and M.-H.L. wrote the paper with R.C.D. and Y. Z.

The authors declare no competing interest.

This article is a PNAS Direct Submission. R.R. is a guest editor invited by the Editorial Board.

Published under the PNAS license.

[1]S.C. and M.-H.L. contributed equally to this work.

[2]To whom correspondence may be addressed. Email: rdynes@ucsd.edu or zhu@bnl.gov.

This article contains supporting information online at https://www.pnas.org/lookup/suppl/doi:10.1073/pnas.2105895118/-/DCSupplemental.

Published September 7, 2021.

Downloaded at PENN STATE UNIV on October 5, 2021

variability is a key issue in developing stochastic neuromorphic networks.

Results and Discussion

Fig. 1*A* illustrates the VO_2/TiO_2 system. The 150-nm VO_2 thin film grows epitaxially on the (001) TiO_2 substrate by radio frequency magnetron sputtering, since rutile VO_2 (R VO_2) and rutile TiO_2 (R TiO_2) share very close in-plane lattice constants (as illustrated in *SI Appendix*, Fig. S1). The selected area electron diffraction (SAED) patterns for R VO_2 and R TiO_2 are shown in *SI Appendix*, Fig. S2 and demonstrate the single-phase growth of the VO_2 film. The R–T curve of as-deposited VO_2 shows an IMT at T_{IMT} ~340 K, with at least three orders of magnitude change in the electrical resistance (*SI Appendix*, Fig. S3*A*). In addition, the single-phase growth of the VO_2 thin film on (001) TiO_2 is also confirmed by the X-ray diffraction (XRD) scan shown in *SI Appendix*, Fig. S3*B*.

To study the electrical properties of in-plane VO_2 devices, an SiO_2 layer was deposited by plasma-enhanced chemical vapor deposition (PECVD) method on the top of VO_2 as an insulating protection layer. The focused ion beam (FIB) lift-out method was taken to make cross-section samples for both *operando* TEM studies and electrical measurements. To apply electrical stimuli through the planar VO_2 devices, 3-mm-diameter semicircle chips with Au pads were used, as shown in the lower portion of Fig. 1*A*. The on-chip Au pads were wire-bonded to the electrical feedthroughs on our customized biasing TEM holder. The electric field was applied onto VO_2 along the in-plane direction via two Pt electrodes, which were deposited during the FIB sample preparation process.

Fig. 1*B* presents ex situ R–T measurement of a TEM device using a probe station. This clearly shows that the VO_2 layer conserves its IMT behavior with a transition temperature of ~335 K. The current–voltage (IV) measurement displayed in Fig. 1*C* shows a volatile resistive switching at room temperature. The IV curves that were measured at least 150 times confirm the device's endurance. Statistical results of the threshold voltage (V_{th}) distribution are shown in Fig. 1*D*. The slight V_{th} difference between each IV cycle shows the electrical stochasticity during the metal–insulator transition within the VO_2 device. Moreover, there were some variations between each cycle in IV curves. To elucidate this, we extracted the initial resistance (the resistance value under very low current density at room temperature) of M1 VO_2 between each IV switching (as shown in Fig. 1*E*). Interesting effects were observed: The initial resistance of M1 VO_2 varies slightly for each IV cycle. The mean value is about 5,020 Ω with ±30-Ω variance. Based on the *operando* TEM measurements, which will be discussed later, we attribute this variance to randomly formed insulating M1 VO_2 domains after each IV measurement. The structural stochasticity places an important effect on the electrical stochasticity of VO_2 due to the coupling between IMT and the structural phase transition.

To understand the underlying physics behind the volatile switching and the resistance variance, TEM characterizations have been carried out. Fig. 2*A* is a high-angle annular dark-field scanning TEM (HAADF-STEM) image from a TEM chip (as illustrated in the lower portion of Fig. 1*A*), showing the cross-section view of the film. The SAED pattern acquired from VO_2 thin film at room temperature is presented in Fig. 2*B*, where three sets of patterns are present. We note that the diffraction patterns were acquired under no biasing, showing the basic structural information of monoclinic VO_2 domains in the in-plane device. Besides the pattern from M1 VO_2 along the [102] zone axis shown in blue

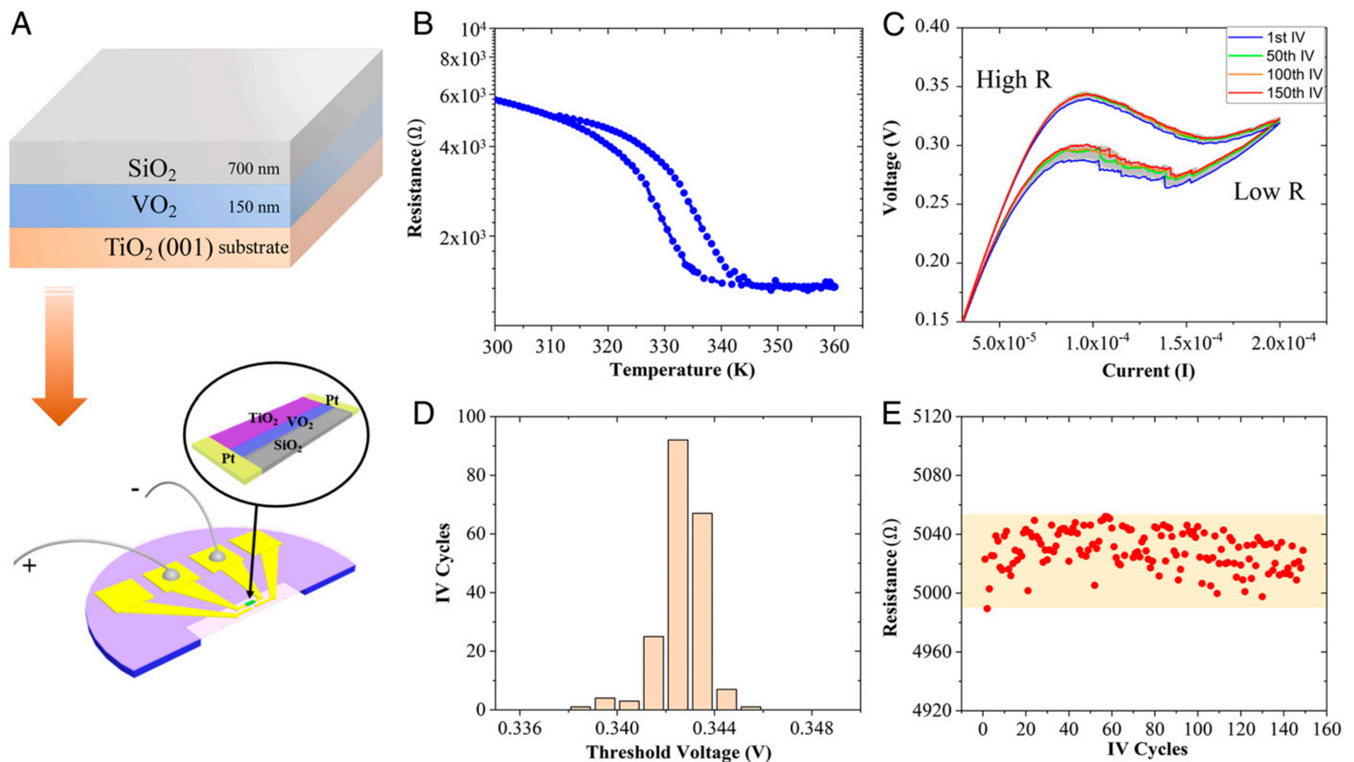

Fig. 1. Ex situ measurement of volatile resistive switching in a VO_2/TiO_2 planar TEM device. (*A*) Schematic of the $SiO_2/VO_2/ TiO_2$ thin film system. The thickness of each layer is indicated. The TEM device schematic is shown at the bottom. The TEM sample fabricated by FIB is enlarged for clarity. The electric field was applied between two Pt electrodes, forming a two-terminal planar device. (*B*) Resistance vs. temperature curve measured from the VO_2 TEM device. (*C*) One hundred fifty voltage–current loops measured from the same device at room temperature. (*D*) Statistical distribution of the threshold voltage (V_{th}). (*E*) The initial resistance values (at T = 300 K) for the M1 phase VO_2 for 150 cycles on the same device at room temperature. The current was fixed to 2.6×10^{-5} A (current density ~1×10^{-14} A/m^2).

Downloaded at PENN STATE UNIV on October 5, 2021

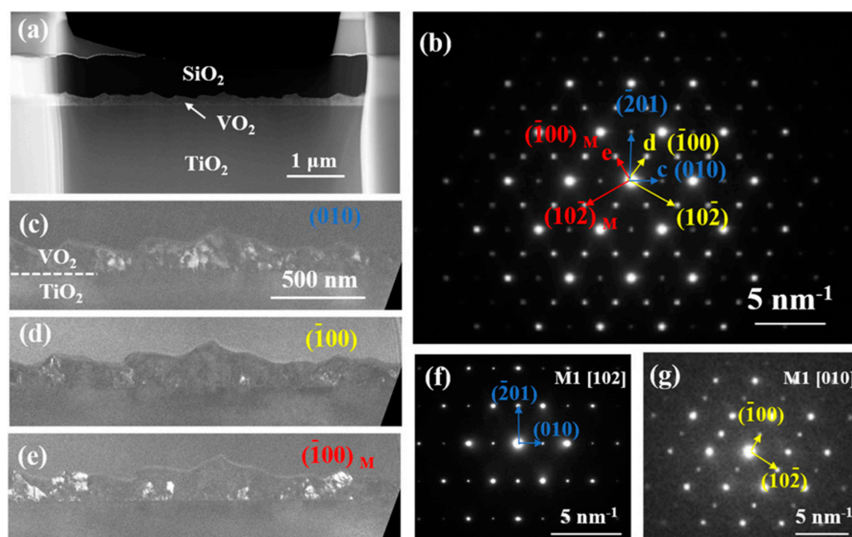

Fig. 2. TEM characterizations of the VO_2/TiO_2 device without biasing. (*A*) A cross-section HAADF-STEM image of an FIB sample. (*B*) The SAED pattern from the sample showing the coexistence of the multiple M1 VO_2 domains. The blue arrows mark the two base vectors for the VO_2 domain at the [102] direction, while the yellow and red arrows indicate the two sets of base vectors for VO_2 domains along the [010] zone axis with mirror symmetry (mirror planes are $\{110\}_{R\ VO2}$). The mirror spot of $(\bar{1}00)$ is indicated as $(\bar{1}00)_M$. (*C–E*) Dark-field images using (010) $(\bar{1}00)(\bar{1}00)_M$diffraction spots from blue, yellow, red base vectors, respectively. (*F* and *G*) SAED patterns for M1 VO_2 along the [102] and [010] directions captured from single domains.

(the diffraction pattern from the [102] zone axis acquired from a single domain is shown in Fig. 2*F*), two mirrored patterns along the [010] direction are indicated by red and yellow arrows (the diffraction pattern from [010] zone axis acquired from a single domain is shown in Fig. 2*G*). The mirror planes are {110} planes of R VO_2, and the mirror spot of $(\bar{1}00)$ is indicated as $(\bar{1}00)_M$. For comparison, the simulated electron diffraction patterns are shown in *SI Appendix*, Fig. S4. The dark-field TEM (DF-TEM) images using the spots **c** [(010) spot from the [102] zone axis], **d** [$(\bar{1}00)$spot from the [010] zone axis], and **e** [$(\bar{1}00)_M$spot from the [010] zone axis] in Fig. 2*B* are illustrated in Fig. 2 *C–E*, respectively. From DF-TEM images it can be found that the monoclinic domains are randomly distributed and the sizes are about 100 nm, which is close to the value previously reported (17–19). Based on the analyses above, the structural orientation and the distributions of the VO_2 monoclinic domains in the insulating state (without biasing) can be well-defined and understood.

In situ biasing TEM experiments have been carried out using this planar VO_2 TEM device at room temperature. An SAED pattern acquired from a randomly picked area (circled in yellow) in Fig. 3*A* before conducting the biasing experiments is shown in Fig. 3*B*, which is consistent with the structural characterization in Fig. 2*B*. Using the $(20\bar{1})$ spot from the $[102]_{M1}$ zone axis (indicated by red arrow), the DF-TEM image is shown in Fig. 3*A*. In the following, we simultaneously acquire SAED pattern from the yellow area and apply a voltage bias. With 1-V biasing across the planar VO_2 device (above the threshold), the diffraction pattern changes from Fig. 3*B* to Fig. 3*D*, which is consistent with the simulated diffraction pattern from R VO_2 [100] (*SI Appendix*, Fig. S4). There was no obvious contrast in the acquired DF-TEM image as shown in Fig. 3*C*, with the position of the objective-lens aperture unchanged. After removing the external biasing, the VO_2 comes back to a monoclinic phase as the diffraction pattern in Fig. 3*F* demonstrates. The two mirrored patterns along the $[010]_{M1}$ direction can be observed and the distribution of the M1 VO_2 phase along the [102] zone axis has changed. Another set of experiments has been conducted and the results are shown in Fig. 3 *G–J*. Although the diffraction pattern in Fig. 3*H* (bias = 1 V) is identical to the one in Fig. 3*D*, demonstrating once again the phase change during the resistive switching, this time, when the bias is removed, the diffraction pattern of the monoclinic insulating phase in Fig. 3*J* is not similar to Fig. 3*F*, but close to that of Fig. 3*B*. The distribution of [102] domains has been altered. Based on the analyses, we have demonstrated that the orientation of the M1 VO_2 can be changed and stabilized in a random fashion. The electron energy-loss spectra acquired from M1 VO_2 and R VO_2 are acquired and presented in *SI Appendix*, Fig. S5*A*, from which the band structure for the two VO_2 phases can be deduced.

The electrical and structural stochasticity can be explained by taking the phase transition pathways between M1 VO_2 and R VO_2 into account. Considering the space groups of rutile metallic VO_2 ($P4_2/mnm$) and monoclinic insulating VO_2 ($P2_1/c$), four possible phase transition pathways are shown in *SI Appendix*, Fig. S6 (20). Four monoclinic variants [M1 (1) to M1 (4)] with 90° rotation symmetry can be found. The relationship of the coordinate systems between M1 (4) phase (the fourth variant) and R phase is illustrated in Fig. 4*A* and can be described by using the following transformation matrix:

$$\begin{bmatrix} a \\ b \\ c \end{bmatrix}_{M1(4)} = \begin{bmatrix} 0 & 0 & 2 \\ 1 & 0 & 0 \\ 0 & 1 & \bar{1} \end{bmatrix} \begin{bmatrix} a \\ b \\ c \end{bmatrix}_R .$$

Thus, $[010]_{M1}$ is parallel to $[100]_R$, and $[102]_{M1}$ is parallel to $[010]_R$. In the R VO_2, both $[100]_R$ and $[010]_R$ are equivalent, while in M1 VO_2, $[010]_{M1}$ and $[102]_{M1}$ are inequivalent, and the in-plane anisotropy is expected. Each time when the VO_2 structure changes from R phase to M1 phase the $[100]_R$ or $[010]_R$ of R VO_2 will randomly turn into either $[010]_{M1}$ or $[102]_{M1}$, which could explain our TEM observations that the distribution of the [010] and [102] domains changes during each IV measurement. Under biasing, the R VO_2 structure will follow that of the R TiO_2 substrate, and there is no in-plane structural anisotropy for R VO_2, whereas the in-plane anisotropy in the monoclinic phase will be induced after the rutile-to-monoclinic structural phase transition. Based on the analysis, there are four variants for M1 VO_2 as shown in *SI Appendix*, Fig. S6, but only three can be observed in Fig. 2*B*, because M1 (3) and M1 (4) are coincident along the observation direction. Also, M1 (1) and M1 (2) appear as the twin structure in Fig. 2*B*.

The electrical stochasticity behavior shown in Fig. 1 and the structural stochasticity of M1 VO_2 structure can be further verified

Downloaded at PENN STATE UNIV on October 5, 2021

https://doi.org/10.1073/pnas.2105895118

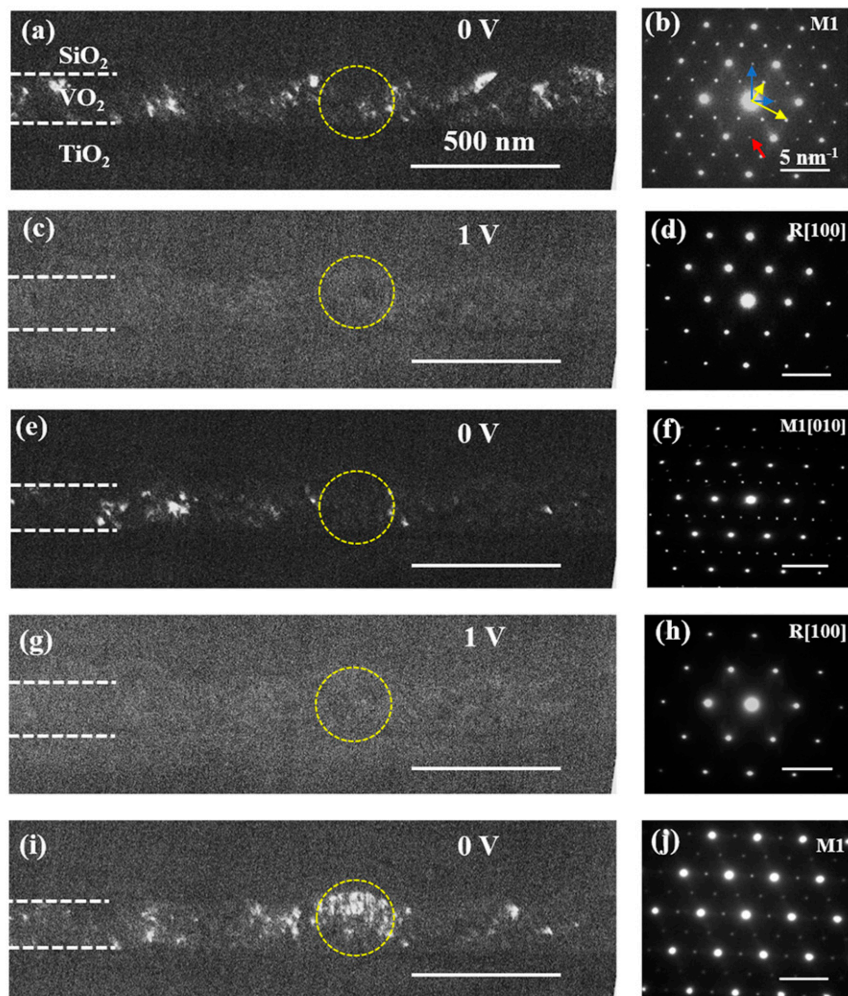

Fig. 3. *Operando* DF-TEM studies for the VO_2 monoclinic/rutile domain evolution during resistive switching. (*A*) DF-TEM image using the diffraction spot indicated by the red arrow in *B* before biasing is applied. (*B*) SAED pattern acquired from the yellow dotted areas in *A*. (*C*) DF-TEM image with 1-V electric biasing applied. (*D*) SAED pattern under 1-V biasing demonstrating that M1 VO_2 changed to R VO_2. (*E*) DF-TEM image taken after the removal of the biasing. (*F*) SAED pattern showing the VO_2 changed to M1 [010]. (*G*) DF-TEM with 1-V electric biasing and M1 VO_2 changed to R VO_2 as indicated in *H*. (*I*) DF-TEM taken after removing external biasing. (*J*) SAED pattern acquired from the yellow region. The same diffraction spot and objective-lens aperture position are used for all the DF-TEM images.

by density functional theory (DFT) calculations. The critical points of the M1 VO_2 first Brillouin zone are shown in Fig. 4*B* (21, 22). The $[010]_{M1}$ and $[102]_{M1}$ are along Γ-Z and Γ-B, respectively. To maintain a consistent k-point density, we relaxed the high-temperature R phase with a monoclinic basis based on the low-temperature phase. The calculated band structures are shown in *SI Appendix*, Fig. S7 *C* and *D*, which is consistent with the published results (23). The gap between the highest occupied energy state of the valence band and the lowest unoccupied state of the conduction band is 0.6 eV. The band structure and density of states (DoS) along Γ-Z and Γ-B for both M1 VO_2 are shown in Fig. 4 *C* and *D*. The band gaps along $[010]_{M1}$ and $[102]_{M1}$ are 0.689 eV and 0.702 eV, respectively, while there is no band gap for R VO_2 (the details for the R VO_2 band gap can be found in *SI Appendix*, Fig. S7 *A* and *B*).

The difference of the band gaps along $[010]_{M1}$ and $[102]_{M1}$ explains the variance of the resistance shown in Fig. 1*E*. It is known that the conductivity of an intrinsic semiconductor is related to the band gap. The intrinsic conductivity in terms of the band gap E_g is $\sigma(T) = \sigma_o \exp(-E_g/2k_bT)$. From this, the conductivity ratio can be calculated as $\sigma[102]_{M1}/\sigma[010]_{M1} \sim 1.286$. Here we neglect the resistance change at the domain walls (including twinning planes), because the domain walls are more metallic than the domains (24). Since the resistances of $[102]_{M1}$ and $[010]_{M1}$ are different, the different ratio of M1 domains among the four crystallographic variants could lead to resistance variation in the insulating state of the VO_2 device. This produces the intrinsic stochasticity in both electronic and structural properties. It may be worthwhile to mention that the estimated conductivity ratio between two directions applies when the physical size of the sample is small and/or the sample switches between the single $[102]_{M1}$ domain and the single $[010]_{M1}$ domain. However, the VO_2 samples usually contain many domains and the measured variance of the resistance (as shown in Fig. 1) should be smaller. A simple method to estimate the distribution of $[102]_{M1}$ and $[010]_{M1}$, and hence the resistance, is provided in the *SI Appendix*, Fig. S8.

To further understand the structural stochasticity in VO_2, we performed phase-field simulations of the equilibrium domain structures of the VO_2 film. The phase-field model of VO_2 was implemented using a four-dimensional structural order parameter and a four-dimensional electronic order parameter (25–28). In the simulations, we set VO_2 to room temperature and its bottom clamped to the (001) TiO_2 substrate. In this configuration, four M1 variants are energetically degenerate. Two calculated equilibrium multidomain structures are depicted in Fig. 4 *E* and *F*. They evolved from a single (nonequilibrium) R domain by applying different random thermal noises in the order parameters, which mimics the nucleation

Downloaded at PENN STATE UNIV on October 5, 2021

Fig. 4. The calculated band structures of M1 VO_2 and R VO_2. (*A*) The relative coordination systems for M1 (4) VO_2 and R VO_2. $[010]_{M1}$ is parallel to $[100]_R$. (*B*) The first Brillouin zone of M1 VO_2. The critical points are indicated. Γ-B and Γ-Z corresponding to $[102]_{M1}$ and $[010]_{M1}$, respectively. Band structures and project DoS for M1 VO_2 along the (*C*) $[010]_{M1}$ and (*D*) $[102]_{M1}$ directions. A legend is provided with the blue dashed and black solid lines being the down and up spin states of the band structure, respectively, and the blue solid and red solid lines being the O and V states of the DoS, respectively. (*E* and *F*) Phase-field calculations on two equilibrium domain structures that evolved from the R phase with different thermal noises in order parameters. The *z* axis is along the out-of-plane direction. The domain wall areas are shown in white.

and growth of M1 domains after different IV cycles, showing the random distribution of the M1 variants.

It is important to consider this intrinsic stochasticity when incorporating neuromorphic devices into the large-scale computing systems. Stochastic behavior is present in the human brain from the single-cell to the network level, and it plays a key role in neuronal firing and signal processing. This biological stochasticity is due to a variety of factors such as channel noise in the ionic conductance (29, 30) or random charged carrier motion in cells, and it can be mimicked by electrical noise during signal transcription and translation in artificial neuron spiking (29, 31).

Stochastic switching may be used to emulate the probabilistic spiking of biological neurons, an important issue for the analysis of sensory stimuli and uncertainty quantification (32). Another possible application is using VO_2 to generate true random numbers (33). Alternatively, the inherent stochasticity would allow the related binary devices to act as error-tolerant schemes (16). Instead of using the excess voltage (much higher than V_{th}) to achieve large switching probabilities, we could take advantage of this inherent stochasticity and use moderate external stimuli to trigger these binary (on and off states) devices, which can be used as the fundamental elements for error-tolerant neuromorphic computing (such as stochastic computing and/or "analog" computing) (16, 34).

In addition, it is also possible to control this intrinsic stochasticity, for example, by implanting ions into VO_2, since this stochasticity is related with the sizes and distributions of M1 domains. There is evidence in the literature that high-energy oxygen implantation reduces the temperature of the IMT process and broadens it somewhat (35–37). We have performed model calculations of the damage and implant profile for ion implantation technique and conclude that the disorder profile and oxygen distribution are quite inhomogeneous throughout the depth of the VO_2 film, and so these results are not surprising. We suggest damaging with high-energy He ions will result in several differences from oxygen implantation. First, the He ions of equal energy will penetrate mostly through the VO_2 film into the substrate. Helium is chemically benign and so will affect the crystalline ordering of the two phases but will not chemically interact. Second, the carrier scattering will increase as a result of the disorder, resulting in shorter mean free paths and probably reducing the effects of different crystallographic anisotropy. Third, by adding some disorder to the TiO_2/VO_2 interface, it is likely that this would increase the density of nucleation sites in the recrystallization process in returning from the more insulating phase to the metallic phase. If this happens, the crystallite sizes would be expected to be smaller and would probably result in a narrower distribution of the threshold voltages reported in Fig. 1*D*. Alternatively, if the devices were fabricated smaller at a length scale comparable to the crystallite sizes we would expect a larger width distribution.

Conclusions

TEM, electrical transport measurements, and theoretical calculations have been combined to successfully reveal the nanoscale phase transition during the volatile switching in VO_2-based planar devices. Both in situ TEM studies and ex situ device measurements were carried out on the same TEM nanochips, which is a good demonstration of a laboratory-on-chip. We have clearly shown that the randomly picked phase transition pathway (from R VO_2 to four variants of M1 VO_2) will change the fractions of different domains, imposing a nonnegligible influence on the electrical properties, which could lead to the inherent electrical and structural stochasticity. Furthermore, we demonstrated an approach to detect small in-plane anisotropy for the slightly distorted M1 VO_2 structure. Clarifying the roles of in-plane anisotropy and phase transition mechanisms would be of great technological importance not only for future neuromorphic-related applications but also the studies of memristors. Our detailed studies have successfully revealed the structural changes of volatile IMT at nanoscale, which is crucial for spiking-related machine intelligence.

APPLIED PHYSICAL SCIENCES

Downloaded at PENN STATE UNIV on October 5, 2021

Materials and Methods

Thin Film Deposition and Device Fabrication. One hundred fifty-nanometer epitaxial VO_2/TiO_2 (001) thin films were deposited using radio frequency magnetron sputtering from a V_2O_3 target. A 3.6-mtorr Ar/O_2 mix (8% O_2) was used during thin film deposition, and the substrate was ∼615 °C during the growth. XRD measurements were performed using Rigaku SmartLab with Cu Kα radiation ($\lambda = 1.54$ Å). The SiO_2 was deposited by Trion Orion III PECVD system at 400 °C for 5 min. The thickness of SiO_2 was measured to be 700 nm via TEM. TEM in-plane devices were prepared by standard FIB lift-out method. The Au and Pt layers were deposited by sputtering and FIB, respectively. The SiO_2 layer was deposited by the PECVD method.

Electrical Transport Measurement. The measurements were performed in a Lakeshore TTPX probe station with a Keithley 6221 current source and a Keithley 2182A nanovoltmeter with a temperature stage.

TEM Characterizations. The DF-TEM images and electron energy loss spectroscopy spectra were acquired by an FEI Talos F200X TEM operated under 200 kV. The in situ biasing holder was an STM Nanofactory in situ biasing holder with slight customization. The wire bonding connecting chip and holder were conducted by a wedge bonder, Kulicke and Soffa 4526.

DFT Calculations. All DFT (38) calculations were performed using the Vienna Ab initio Simulation Package (VASP) within the projector augmented wave approach (39–41). The exchange-correlation effects were modeled using the Perdew–Berke–Ernzerh of the generalized gradient approximation (GGA) functional (42). The GGA functional is known for being unable to correctly predict electronic properties such as the band structure, band gap, and DoS due to the strong correlation in VO_2 (23). We circumvent this by introducing the Hubbard U parameter with U = 3.06 eV to all calculations of the high-temperature R and low temperature M1 VO_2 phases. The Hubbard U was fitted to obtain a band gap of 0.6 eV in the low-temperature monoclinic phase of VO_2 in accordance with experimentally observed band gaps (43). The pseudopotentials used are similar to those used in the Materials Project (44). The energies and atomic forces of all calculations were converged within 10^{-5} eV and 0.01 eVÅ^{-1}, respectively, and a plane wave cutoff energy of 900 eV was used. Γ-centered k-point meshes of $9 \times 9 \times 9$ were used in calculating the DoS. Analysis of DoS and band structure was performed with the aid of the Python Materials Genomics (Pymatgen) materials analysis library (45). The high-symmetry K-path of the band structure was obtained using the method described by Setyawan and Curtarolo (46).

Data Availability. All study data are included in the article and/or *SI Appendix*.

ACKNOWLEDGMENTS. This work (synthesis, structural characterization, transport, theoretical calculations, and the collaboration between Brookhaven National Laboratory (BNL) and the University of California San Diego) was supported as part of Quantum Materials for Energy Efficient Neuromorphic Computing (Q-MEEN-C), an Energy Frontier Research Center funded by the US Department of Energy (DOE), Office of Science, Basic Energy Sciences (BES) under Award DE-SC0019273. Electron microscopy at BNL and the use of BNL's Center for Functional Nanomaterials are supported by DOE-BES, the Division of Materials Science and Engineering, and Division of Science User Facility, respectively, under contract DE-SC0012704. R.T. and S.P.O. acknowledge computational resources provided by Triton Shared Computing Cluster at the University of California San Diego. The phase-field modeling was supported as part of the Computational Materials Sciences Program funded by the US DOE, Office of Sciences, BES, under award DE-SC0020145.

1. J. D. Valle, J. G. Ramírez, M. J. Rozenberg, I. K. Schuller, Challenges in materials and devices for resistive-switching-based neuromorphic computing. *J. Appl. Phys.* **124**, 211101 (2018).
2. W. Yi *et al*., Biological plausibility and stochasticity in scalable VO_2 active memristor neurons. *Nat. Commun.* **9**, 4661 (2018).
3. D. Ielmini, H.-S. P. Wong, In-memory computing with resistive switching devices. *Nat. Electron.* **1**, 333 (2018).
4. Z. Yang, C. Ko, S. Ramanathan, Oxide electronics utilizing ultrafast metal-insulator transitions. *Annu. Rev. Mater. Res.* **41**, 337 (2011).
5. F. Morin, Oxides which show a metal-to-insulator transition at the Neel temperature. *Phys. Rev. Lett.* **3**, 34 (1959).
6. J. Del Valle *et al*., Subthreshold firing in Mott nanodevices. *Nature* **569**, 388–392 (2019).
7. Y. Kalcheim *et al*., Non-thermal resistive switching in Mott insulator nanowires. *Nat. Commun.* **11**, 2985 (2020).
8. S. Cheng *et al*., *Operando* characterization of conductive filaments during resistive switching in Mott VO_2. *Proc. Natl. Acad. Sci. U.S.A.* **118**, e2013676118 (2021).
9. A. G. Shabalin *et al*., Nanoscale imaging and control of volatile and non-volatile resistive switching in VO_2. *Small* **16**, e2005439 (2020).
10. W. Sun *et al*., Understanding memristive switching via in situ characterization and device modeling. *Nat. Commun.* **10**, 3453 (2019).
11. Z. Shao, X. Cao, H. Luo, P. Jin, Recent progress in the phase-transition mechanism and modulation of vanadium dioxide materials. *NPG Asia Mater.* **10**, 581–605 (2018).
12. J. Kim, C. Ko, A. Frenzel, S. Ramanathan, J. E. Hoffman, Nanoscale imaging and control of resistance switching in VO_2 at room temperature. *Appl. Phys. Lett.* **96**, 213106 (2010).
13. A. Sharoni, J. G. Ramírez, I. K. Schuller, Multiple avalanches across the metal-insulator transition of vanadium oxide nanoscaled junctions. *Phys. Rev. Lett.* **101**, 026404 (2008).
14. T. S. Kasırga *et al*., Photoresponse of a strongly correlated material determined by scanning photocurrent microscopy. *Nat. Nanotechnol.* **7**, 723–727 (2012).
15. M. A. Kats *et al*., Vanadium dioxide as a natural disordered metamaterial: Perfect thermal emission and large broadband negative differential thermal emittance. *Phys. Rev. X* **3**, 041004 (2013).
16. S. Gaba, P. Sheridan, J. Zhou, S. Choi, W. Lu, Stochastic memristive devices for computing and neuromorphic applications. *Nanoscale* **5**, 5872–5878 (2013).
17. J. D. Valle *et al*., Resistive asymmetry due to spatial confinement in first-order phase transitions. *Phys. Rev. B* **98**, 045123 (2018).
18. W. Fan *et al*., Large kinetic asymmetry in the metal-insulator transition nucleated at localized and extended defects. *Phys. Rev. B Condens. Matter Mater. Phys.* **83**, 235102 (2011).
19. J. Wu *et al*., Strain-induced self organization of metal-insulator domains in single-crystalline VO_2 nanobeams. *Nano Lett.* **6**, 2313–2317 (2006).
20. A. Tselev *et al*., Symmetry relationship and strain-induced transitions between insulating M1 and M2 and metallic R phases of vanadium dioxide. *Nano Lett.* **10**, 4409–4416 (2010).
21. Y. Hinuma, G. Pizzi, Y. Kumagai, F. Oba, I. Tanaka, Band structure diagram paths based on crystallography. *Comput. Mater. Sci.* **128**, 140 (2017).
22. A. Togo, I. Tanaka, Spglib: A software library for crystal symmetry search. arXiv [Preprint] (2018). https://arxiv.org/abs/1808.01590 (Accessed 4 January 2020).
23. Z. Zhu, U. Schwingenschlögl, Comprehensive picture of VO_2 from band theory. *Phys. Rev. B Condens. Matter Mater. Phys.* **86**, 2–5 (2012).
24. A. Tselev *et al*., Mesoscopic metal-insulator transition at ferroelastic domain walls in VO_2. *ACS Nano* **4**, 4412–4419 (2010).
25. Y. Shi, F. Xue, L.-Q. Chen, Ginzburg-Landau theory of metal-insulator transition in VO_2: The electronic degrees of freedom. *Europhys. Lett.* **120**, 46003 (2017).
26. Y. Shi, L.-Q. Chen, Phase-field model of insulator-to-metal transition in VO_2 under an electric field. *Phys. Rev. Mater.* **2**, 053803 (2018).
27. Y. Shi, L.-Q. Chen, Current-driven insulator-to-metal transition in strongly correlated VO_2. *Phys. Rev. Appl.* **11**, 014059 (2019).
28. Y. Shi, L.-Q. Chen, Spinodal electronic phase separation during insulator-metal transitions. *Phys. Rev. B* **102**, 195101 (2020).
29. J. A. White, J. T. Rubinstein, A. R. Kay, Channel noise in neurons. *Trends Neurosci.* **23**, 131–137 (2000).
30. R. C. Cannon, C. O'Donnell, M. F. Nolan, Stochastic ion channel gating in dendritic neurons: Morphology dependence and probabilistic synaptic activation of dendritic spikes. *PLOS Comput. Biol.* **6**, e1000886 (2010).
31. M. R. Mahmoodi, M. Prezioso, D. B. Strukov, Versatile stochastic dot product circuits based on nonvolatile memories for high performance neurocomputing and neurooptimization. *Nat. Commun.* **10**, 5113 (2019).
32. K. Wang *et al*., Threshold switching memristor-based stochastic neurons for probabilistic computing. *Mater. Horiz.* **8**, 619 (2021).
33. M. Jerry, K. Ni, A. Parihar, A. Raychowdhury, S. Datta, Stochastic insulator-to-metal phase transition based true random number generator. *IEEE Electron Device Lett.* **39**, 139–142 (2017).
34. Y. Yang, W. Lu, Nanoscale resistive switching devices: Mechanisms and modeling. *Nanoscale* **5**, 10076–10092 (2013).
35. R. Lopez, L. A. Boatner, T. E. Haynes, Enhanced hysteresis in the semiconductor-to-metal phase transition of VO_2 precipitates formed in SiO_2 by ion implantation. *Appl. Phys. Lett.* **79**, 3161 (2001).
36. K.-D. Ufert, Doping of VO_2 thin films by ion implantation. *Phys. Status Solidi, A Appl. Res.* **42**, 187–190 (1977).
37. J. G. Ramirez *et al*., Effect of disorder on the metal-insulator transition of vanadium oxides: Local versus global effects. *Phys. Rev. B Condens. Matter Mater. Phys.* **91**, 205123 (2015).
38. G. Kresse, J. Hafner, *Ab initio* molecular dynamics for liquid metals. *Phys. Rev. B Condens. Matter* **47**, 558–561 (1993).
39. W. Kohn, L. J. Sham, Self-consistent equations including exchange and correlation effects. *Phys. Rev.* **140**, 1133–1138 (1965).
40. P. E. Blöchl, Projector augmented-wave method. *Phys. Rev. B Condens. Matter* **50**, 17953–17979 (1994).
41. G. Kresse, J. Furthmüller, Efficient iterative schemes for ab initio total-energy calculations using a plane-wave basis set. *Phys. Rev. B Condens. Matter* **54**, 11169–11186 (1996).
42. J. P. Perdew, K. Burke, M. Ernzerhof, Generalized gradient approximation made simple. *Phys. Rev. Lett.* **77**, 3865–3868 (1996).
43. A. Zylbersztejn, N. F. Mott, Metal-insulator transition in vanadium dioxide. *Phys. Rev. B* **11**, 4383–4395 (1975).
44. A. Jain *et al*., Commentary: The Materials Project: A materials genome approach to accelerating materials innovation. *APL Mater.* **1**, 0110021 (2013).
45. S. P. Ong *et al*., Python Materials Genomics (pymatgen): A robust, open-source python library for materials analysis. *Comput. Mater. Sci.* **68**, 314–319 (2013).
46. W. Setyawan, S. Curtarolo, High-throughput electronic band structure calculations: Challenges and tools. *Comput. Mater. Sci.* **49**, 299–312 (2010).

Downloaded at PENN STATE UNIV on October 5, 2021